Atmospheric Research 214 (2018) 204–212

Contents lists available at ScienceDirect

Atmospheric Research

journal homepage: www.elsevier.com/locate/atmosres

Characteristics of the planetary boundary layer above Wuhan, China based on CALIPSO

Zhongmin Zhu[a,b,1], Miao Zhang[c,a], Yusi Huang[b,*], Bo Zhu[d,*], Ge Han[e], Tianhao Zhang[b], Boming Liu[b]

[a] Wuchang Shouyi University, Wuhan 430064, China
[b] State Key Laboratory of Information Engineering in Surveying, Mapping, and Remote Sensing, Wuhan University, 129 Luoyu Road, Wuhan 430079, China
[c] School of Environmental Science and Tourism, Nanyang Normal University, Wolong Road No. 1638, Nan Yang 473061, China
[d] Hubei Provincial Environmental Monitoring Center Station (B.Z), China
[e] School of Remote Sensing and Information Engineering, Wuhan University, Wuhan 430079, China

ARTICLE INFO

Keywords:
Planetary boundary layer
CALIPSO
Aerosol

ABSTRACT

Planetary boundary layer height (PBLH) has important implications for human health, weather forecasting, ecology, and climate change. This study aims to investigate the characteristics of the PBLH above Wuhan, China. We propose a new procedure (wavelet covariance and the ideal curve-fitting algorithm) to reveal PBLHs based on the Cloud-Aerosol LIDAR and Infrared Pathfinder Satellite Observations (CALIPSO) attenuated backscatter ratio. Under cloud situation, the results of PBLHs revealed from CALIPSO show a relatively low correlation (R^2 = 0.55) with PBLHs determined using a thermodynamic method. And the results show a significant correlation coefficient (R^2 = 0.86) when the cloudy scenarios are eliminated. Because CALIPSO could have mistakenly classified cloud tops as PBLHs during the formation of stratocumulus clouds. Characteristics of annual and seasonal variations of the PBLH for all sky conditions from June 2006 to September 2013 were also studied. Because of the climatic and geographic characteristics of Wuhan City, the PBLHs display clear annual and seasonal variations. Warmer seasons have deeper PBLHs, while colder seasons are characterized by shallower PBLHs. Over 90% of daytime PBLHs in Wuhan are between 400 and 1800 m, while over 90% of nocturnal PBLHs clustered between 200 m and 1000 m. This research will contribute to improving PBLH input parameters for numerical models and enhance the understanding of the urban planetary boundary layer.

1. Introduction

The planetary boundary layer (PBL) is the lowest part of the atmosphere, ranging from a few tens to thousands of meters in height. As such, it is vital to human life (Garratt, 1994; Chen et al., 2006). Atmospheric momentum, heat, water vapor, and aerosol particles mix thoroughly within the PBL (Stull, 1988). Aerosol particles within the PBL alter the balance of atmospheric radiative transmission by absorbing and scattering solar radiation directly (Russell et al., 1999; Yang et al., 2016; Yang et al., 2017) and indirectly by modifying cloud properties (Twomey, 1977; Kaufman and Fraser, 1997; Garrett and Zhao, 2006; Xie et al., 2013; Zhao and Garrett, 2015; Li et al., 2016). In inland cities, atmospheric pollutants gather within the PBL and higher concentrations of contaminants can result in extreme weather episodes such as fog, haze, and dust in the PBL, which can have severe effects on ecology, climate, and the environment (Garrett et al., 2004; Seinfeld and Pandis, 2012; Zhao et al., 2018).

The PBL height (PBLH) is an important physical quantity and is an input parameter for weather forecasting models. The spatiotemporal characteristics of PBLH evolution have important implications on air quality and weather changes (Tang et al., 2015; Tang et al., 2016; Zhu et al., 2017). Recent studies found that thermal internal boundary layer leaded to the increasing of particular matter in evening owing to its promotion on the rapid accumulation of atmospheric pollutions (Wei et al., 2017), and shallow boundary layer weakened the regional diffusion ability during haze episode period (Zhu et al., 2016). PBLH is usually obtained by three methods: meteorological radiosonde profiles, aeroplane surveying, and remote sensing (Tang et al., 2016). As the

* Corresponding author.
E-mail addresses: zhongmin.zhu@whu.edu.cn (Z. Zhu), zm_liesmars@whu.edu.cn (M. Zhang), mavis_huang@whu.edu.cn (Y. Huang), zhubo125@whu.edu.cn (B. Zhu), udhan@whu.edu.cn (G. Han).
[1] These authors contributed equally to this work.

https://doi.org/10.1016/j.atmosres.2018.07.024
Received 8 January 2018; Received in revised form 26 June 2018; Accepted 31 July 2018
Available online 01 August 2018
0169-8095/ © 2018 Elsevier B.V. All rights reserved.

most commonly used method, meteorological radiosonde profiles are based on the thermodynamic characteristics of the atmosphere (temperature flux, humidity flux, wind shear, tec.), but, the low temporal resolution (usually twice a day) makes it impossible to detect the change of the boundary layer, the turbulent and fluctuating characteristic of boundary layer in small time scale (Seibert et al., 2000). Although aeroplane surveying can obtain higher temporal resolution data in favor of studying the change and characteristic of the boundary layer, the constraints of air traffic control, weather conditions, and surveying cost reduce the counts of experiment samples (Tang et al., 2016). Therefore, due to the significant advantage of having high temporal and vertical resolutions, remote sensing is gradually adopted to detect PBLH. Doppler radar based on the wind characteristic, has been used to obtain PBLH by detecting the turbulent structure of the boundary layer, but is easily interfered by clouds (Bianco and Wilczak, 2002). Sodar based on acoustic properties, can identify PBLH by detecting the position of sudden changes in the vertical profiles of wind and temperature data, but its detection height is lower than 1 km, which is limited to study the PBLH under convection states (Beyrich and Görsdorf, 1995; Emeis et al., 2008). Lidar, as an important part of remote sensing in recent years, has become an effective tool to retrieve PBLH using aerosols as tracers (Baars et al., 2008; Granados-Muñoz et al., 2012; Jordan et al., 2010; McGrath-Spangler and Denning, 2012; Compton et al., 2013; McGrath-Spangler and Denning, 2013; Zhang et al., 2016; Su et al., 2017; Liu et al., 2018), because their concentrations are far higher in the PBL than in the free atmosphere above (Melfi et al., 1985; Donnell et al., 2001; Henne et al., 2004). Accordingly, Lidar backscatter within the PBL is higher than that in the free atmosphere, and the PBLH can be identified through gradient difference in Lidar backscatter (Flamant et al., 1997; Davis et al., 2000; Tang et al., 2015; Tang et al., 2016; Zhu et al., 2017).

Due to its ability to obtain vertical aerosol and cloud information on regional and global scales, Cloud-Aerosol LIDAR and Infrared Pathfinder Satellite Observations (CALIPSO) have been employed to explore the PBLH in recent years (McGrath-Spangler and Denning, 2012; McGrath-Spangler and Denning, 2013; Zhang et al., 2016; Su et al., 2017). Jordan et al. conducted a PBL detection in the Western Hemisphere using CALIPSO data, and adopted satellite-derived PBLHs to evaluate the GEOS-5 MERRA PBLHs. Meanwhile, McGrath-Spangler et al. presented global PBLHs based on CALIPSO backscatter for the first time. Various methods for detecting CALIPSO-derived PBLHs have been proposed, e.g., the vertical variance method (Jordan et al., 2010; McGrath-Spangler and Denning, 2012; McGrath-Spangler and Denning, 2013; Zhang et al., 2016; Su et al., 2017) and the aerosol-layer-top of CALIPSO level-2 aerosol-layer products method (Wu et al., 2010; Leventidou et al., 2013). The long distance of signal transmission can lead to considerable background noise in CALIPSO data causing the signal-to-noise ratio (SNR) of the Level 1B product to be low (Jordan et al., 2010). Therefore, it is important to find a method that is insensitive to noise in order to retrieve PBLHs based on CALIPSO.

In this study, we employ a combined method of wavelet covariance transform (WCT) and the ideal curve-fitting (ICF) algorithm to retrieve PBLH based on CALIPSO. WCT is flexible for basis function choice, and relatively simple in implementation (Davis et al., 2000; Brooks, 2003; Morille et al., 2007; Baars et al., 2008; Wu et al., 2010; Granados-Muñoz et al., 2012; Compton et al., 2013; Sawyer and Li, 2013). The ICF algorithm can tolerate more irrelevant noise and is stable when subjected to interference from multi-light layers (Press, 1992; Steyn et al., 1999). In order to evaluate the new method, we employed a microwave radiometer, which can also obtain PBLHs based on atmospheric thermodynamic information with uncuncertainty of a few hundred meters (Seibert et al., 2000; Seidel et al., 2010; Cimini et al., 2013; Korhonen et al., 2014). In addition, the annual and seasonal characteristics of PBLH above Wuhan, China are investigated using three datasets collected between June 2006 and September 2013. Sections 2 and 3 of the paper describe the data used and adopted methods, respectively, Section 4 consists of the results and discussion, and Section 5 presents a brief summary and conclusions.

2. Dataset

2.1. CALIPSO data

Launched on 28 April 2006, CALIPSO is part of the A-train satellite constellation. The Cloud-Aerosol Lidar with Orthogonal Polarization (CALIOP) instrument onboard CALIPSO emits 532-nm and 1064-nm laser pulses vertically downward with a 110-mJ pulse energy. The 532-nm laser is equipped with a polarized channel with a repetition rate of 20.25 Hz and a pulse width of 20 ns. The dataset used in this research contains version 3.01 level 1B data available online from the Atmospheric Science Data Center at NASA Langley Research Center. The vertical resolution of attenuated backscatter data at −0.5 to 8.2 km height is 30 m and the horizontal resolution is 330 m (Winker et al., 2003; Winker et al., 2007). The experiment was performed at the State Key Laboratory of Information Engineering in Surveying, Mapping, and Remote Sensing (LIESMARS) site (30°32′N, 114°21′E, 30 m above sea level) at Wuhan University, Hubei Province, China. The nearest distance of the CALIPSO ground track from the LIESMARS site was < 60 km (Feiyue et al., 2012). As reported by Leventidou et al., a distance of < 90 km will not affect the PBLHs results, allowing a comparison between CALIPSO and other equipment at the LIESMARS site (Leventidou et al., 2013). The CALIPSO has a crossing time of about 0230 and 1430 local zone time (LZT) over Wuhan. The Level 1B signal profiles were averaged to 5-km horizontal resolution to improve the SNR. CALIPSO data were collected from June 2006 to September 2013.

2.2. Microwave radiometer data

In this study, a multichannel microwave radiometer (RPG-HATPRO), manufactured by Radiometer Physics GmbH (Germany), was also employed it to obtain PBLHs. The device is able to provide real-time continuous monitoring of humidity and temperature profiles in the PBL and troposphere. The microwave radiometer can resolve 39 pressure surfaces from 0 to 10 km; the vertical resolution gradually decreases with increasing height. Since the maximum vertical resolution is 10 m at low altitude, more detailed atmospheric information is obtained to detect- low-altitude PBL, which improves the accuracy of detection using the RPG-HATPRO to some extent. The temporal resolution of the microwave radiometer is set at 2 min. Additional information about the instrument can be found in the relevant literature (Cimini et al., 2013). The microwave radiometer was installed in September 2010 at the LIESMAR site. The dataset used in this study covers the period from September 2010 to June 2013 with a temporal resolution of 25 min.

3. Methodology

3.1. CALIPSO PBLH detection

This study introduces a detection method that combines the ICF and WCT algorithms to retrieve CALIPSO-derived PBLH. This method has been used for MPL-derived PBLH detection and its efficacy has been demonstrated (Sawyer and Li, 2013). The ICF algorithm was designed to eliminate interference from multi-light layers and strong noise in the backscattered signals, and is based on the Lidar backscattered ratio profile for detecting the PBLH (Steyn et al., 1999). As shown in Eq. (1), the basic concept of the ICF algorithm is that it uses the Lidar backscattered signal as the actual measured signal b(z). Then, by adopting the ideal profile model B(z) with four pending parameters, and by fitting the entire actual measured signals b(z) into the ideal profile model B(z) according to the least squares principle, four pending unknown parameters B_u, B_m, Z_m, and s are obtained. Among these, Z_m is the

PBLH, s relates to the transport layer, B_m is the average value of the backscatter coefficients within the PBL, and B_u is the average value of the atmospheric backscatter coefficients above the PBL. Furthermore, z is the detection height and erf() is the Gauss error function.

$$B(z) = \frac{B_m + B_u}{2} - \frac{B_m - B_u}{2}\,\mathrm{erf}\left(\frac{z - Z_m}{s}\right) \tag{1}$$

To use the ICF method, the initial estimated values of the above-mentioned four parameters need to be obtained beforehand. The WCT method was adopted in this study to obtain those four initial parameters. The WCT is a refined and common method that has independent, automated, and highly efficient detection functions for many types of datasets, and has few requirements for a priori information such as equipment characteristics or weather conditions (Davis et al., 2000; Brooks, 2003; Morille et al., 2007; Baars et al., 2008; Granados-Muñoz et al., 2012; Compton et al., 2013; Sawyer and Li, 2013). The WCT is defined as:

$$W_f(a,b) = a^{-1}\int_{zb}^{zt} f(z)h\left(\frac{z-b}{a}\right)dz \tag{2}$$

with

$$h\left(\frac{z-b}{a}\right) = \begin{cases} -1 & b - \frac{a}{2} \le z \le b \\ 1 & b \le z \le b + \frac{a}{2} \\ 0 & \text{elsewhere} \end{cases} \tag{3}$$

where zt and zb are the lower and upper limits of the backscattered signal; f(z) represents the intensity of the actual measured signal; the position of the PBLH is indicated when $W_f(a,b)$ reaches its maximum value. The term $h\left(\frac{z-b}{a}\right)$ is the Haar wavelet function, a represents the Haar wavelet dilation scale, b represents the translation of the Haar function, and z represents the height. Physically, a also represents the thickness of the transmission region and the PBLH is the center of a. Sawyer and Li discussed issues concerning the selection of a, declaring that a value for a that is too large or too small would lead to a "plateau" phenomenon in the PBLH (Sawyer and Li, 2013). Based on their research, Mao et al. selected a value of 32 times the vertical resolution for a (Mao et al., 2013). Granados-Muñoz et al. expounded that small a-values can result in a noisy WCT profile while large values may overlook some structures (Granados-Muñoz et al., 2012). Baars et al. stated that a-values between 200 and 450 m could provide good results depending on the Lidar vertical resolution. For the CALIPSO signals in this study, a was set at 300 m (10 times the vertical resolution) (Baars et al., 2008). The WCT method is used as the initial estimate of Z_m (initial PBLH) in the ICF method. Initial estimates of B_m and B_u are the mean backscatter values above and below the Z_m, respectively. The initial estimate of s is the aforementioned a. Thus, the ICF method will take the initial estimates determined by the WCT method as the starting point to perform the PBLH detection based on the "simulated annealing" algorithm.

Furthermore, to eliminate the effects of the atmospheric molecular scattering to highlight the characteristics of the PBL, the attenuated backscatter ratio R(z) signals of CALIPSO were adopted as measured signals b(z) in this study. We know from Eq. (4) that:

$$\beta_{total}(z) = \beta_{\perp}(z) + \beta_{||}(z) = [\beta_p(z) + \beta_m(z)]T_p^2(z)T_m^2(z) \tag{4}$$

where $\beta_{total}(z)$ is the total attenuated backscatter of CALIPSO, $\beta_{\perp}(z)$ and $\beta_{||}(z)$ represent the vertical and horizontal attenuated backscatter of the polarized channels, respectively, $\beta_p(z)$ and $\beta_m(z)$ indicate the backscatter coefficients of aerosol particles and air molecules, respectively, and $T_p^2(z)$ and $T_m^2(z)$ indicate bidirectional transmittance rates of aerosol particles and air molecules, respectively. Similarly, the attenuated backscatter of air molecules can be represented as:

$$\beta_{air}(z) = \beta_m(z)T_m^2(z) \tag{5}$$

Thus, the attenuated backscatter ratio R(z) can be represented as:

$$R(z) = \beta_{total}(z)/\beta_{air}(z) = [1 + \beta_p(z)/\beta_m(z)]T_p^2(z) \tag{6}$$

Here, $\beta_{air}(z)$ was obtained through the commonly adopted U.S. 1976 standard atmosphere model (Krueger and Minzner, 1976) as following:

$$\beta_{air} = \beta_m(z)\,exp\left[-2\int_0^z \alpha_m(z)dz\right] \tag{7}$$

$$\alpha_m(\lambda,z) = \frac{8\pi}{3}\beta_m(\lambda,z) \tag{8}$$

$$\beta_m(\lambda,z) = 0.00154\left(\frac{532}{\lambda}\right)^4 exp\left(\frac{-z}{7}\right) \tag{9}$$

where λ is the wavelength, z is the height of the backscattered signal. The attenuation backscatter ratio R(z) can then be obtained, which highlights only the influence of aerosols. Thus, the accuracy of the PBLH-retrieval algorithm is improved without interference from air molecules and other sources of error.

3.2. Microwave radiometer PBLH detection

Based on about ten years radiosonde data from history observations as a training dataset, the temperature profiles with acceptable uncertainties were retrieved from measured brightness temperatures, using artificial neural networks algorithm (Churnside et al., 1994; Zhao et al., 2012). Using the temperature profile derived from the microwave radiometer, the potential temperature profile can be calculated according to Eq. (7) (Wallace and Hobbs, 2006):

$$\theta = T\left(\frac{1000}{P}\right)^{\frac{AR_d}{C_{pd}}} \tag{10}$$

$$P = P_0 \bullet \left(1 - \frac{L \bullet h}{T_0}\right)^{\frac{g \bullet M}{R_0 \bullet L}} \tag{11}$$

Since the microwave radiometer can only obtain the pressure data on the surface, we calculated the pressure data in different levels according to the barometric formula (Eq. (8)) (Quick, 2004). Where T and P represent air temperature and pressure at any height, A represents the mechanical equivalent of heat, R_d is the gas constant of dry air, and C_{pd} is the specific heat of dry air at constant pressure, P_0 represents the sea level standard atmospheric pressure; L represents the temperature lapse rate for dry air; h is the altitude; T_0 is the sea level standard temperature; g is Earth-surface gravitational acceleration; M is the molar mass of dry air; R_0 is universal gas constant. In this study, we also employed the ICF-WCT method proposed by Sawyer and Li (2013) to detect the PBLH using the temperature profile derived from the microwave radiometer.

The aerosols are roughly uniformly distributed within PBL and have a sharp decrease above the PBLH (Zheng and Zhao, 2017; Zhao et al., 2018), which provide the basis for determination of PBLH based on lidar backscattering signals. Different to the Lidar technique based on the vertical concentration and gradient changes of aerosols, PBLH detection using radiometer is based on the thermodynamic properties of the atmosphere. Thus, the correlations and differences between thermodynamic factors and aerosol indicators in PBLH detection could be revealed. As shallower PBLs have greater convectional reactions that develop towards the relatively stable free atmosphere above, the position of the maximum vertical gradient of potential temperature (θ) can be used as the PBLH (Stull, 1988; Garratt, 1994). The relative humidity or minimum position of the vertical gradient of absolute humidity are also often used as the PBLH, because the concentration of vapor within the PBL is well mixed and often greater than that in the free atmosphere

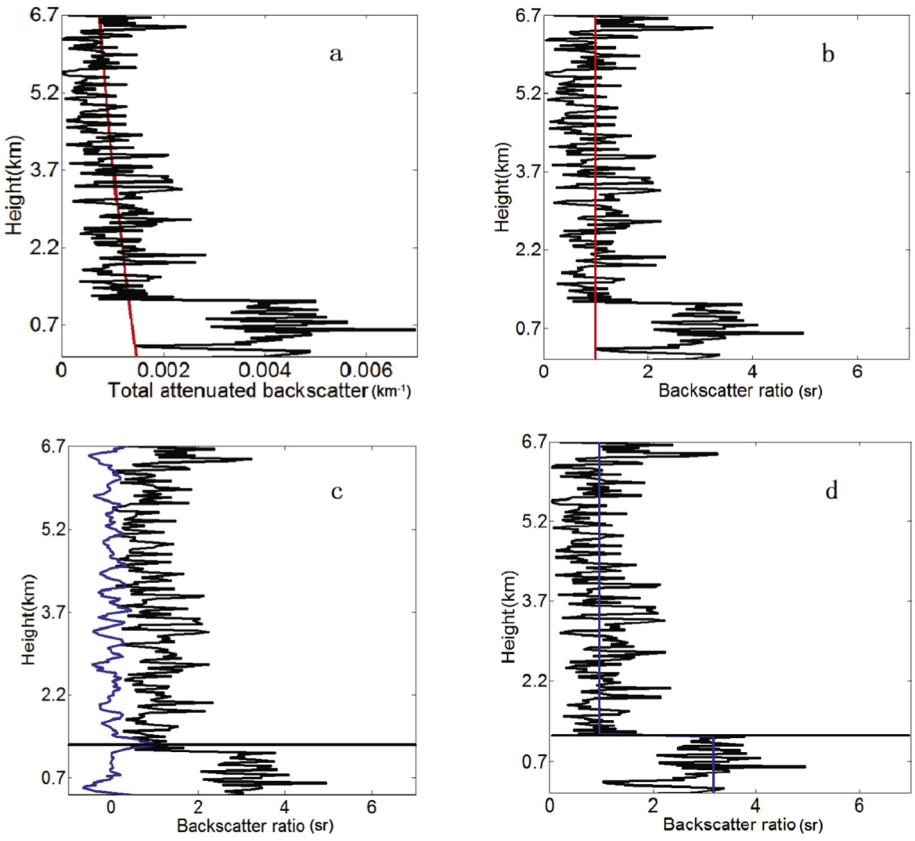

Fig. 1. (a) Atmospheric molecule backscatter (red line) and CALIPSO total attenuated backscatter (black line); (b) atmospheric molecule backscatter (red line) and CALIPSO attenuated backscatter ratio (black line); (c) result of the Haar wavelet covariance (blue line) and CALIPSO attenuated ratio (black line); (d) result of the new algorithm (blue line) and CALIPSO attenuated ratio (black line). (For interpretation of the references to colour in this figure legend, the reader is referred to the web version of this article.)

above. The wavelet curve-fitting method proposed by Sawyer and Li (2013) is used for the θ profile for the microwave radiometer. However, the basic Haar function of the wavelet is changed to

$$h\left(\frac{z-b}{a}\right)=\begin{cases}1 & b-\frac{a}{2}\le z\le b\\ -1 & b\le z\le b+\frac{a}{2}\\ 0 & \text{elsewhere}\end{cases} \quad (12)$$

The algorithm defines the PBLH as the center height of the stratospheric vertical θ profile (Stull, 1988). This algorithm locates the position where θ rises rapidly, which lies between the nearly homogeneous mixed layer and the more stable free atmosphere above. Using the thermodynamic profile as a total profile is effective for locating the stratosphere and the performance is stable.

4. Results and discussion

4.1. Analysis of the correlation coefficient

Fig. 1 displays the performance of the WCT-ICF method using CALIPSO attenuated backscatter data. Fig. 1 (a) and (b) compare the distribution of atmospheric molecule backscatter between using total attenuated backscatter of CALIPSO directly and using the attenuated backscatter ratio calculated based on the method mentioned above. Fig. 1 (c) and (d) compare the detection results of Harr wavelet covariance and WCT-ICF algorithm. The solid black line in Fig. 1(a) is the result of the total attenuated backscatter of CALIPSO level 1B data, while the solid black line in Fig. 1 (b), (c), and (d) represent the attenuated backscatter ratio calculated using the methods mentioned above. The red line in Fig. 1 (a) and (b) indicate the backscatter of atmospheric molecules, and the blue line in Figure (c) indicates the results of the Haar wavelet covariance while the blue line in Fig. 1 (d) is the results of WCT-ICF algorithm. It can be seen that the signal amplitude of the total attenuation backscatter in Fig. 1 (a) is larger, and the total energy of signals is increased by noise and air molecules, resulting in a tilted shape that is consistent with the distribution of the molecules. In Fig. 1 (b), when the influence of the molecules is eliminated, the shape becomes vertical and the aerosol characteristics in the PBL become prominent (Zhao et al., 2014). Fig. 1(c) shows the initial estimated values obtained by the Haar wavelet method. Fig. 1(d) presents the PBLH obtained using the new method. Compared to the WCT method, the new algorithm well separated the upper and low parts of PBL. Fig. 2 illustrates the 2D energy intensity distribution of the CALIPSO attenuated backscatter ratio. The black solid line is the PBLHs based on the new method. The figure clearly illustrates that our method is able to distinguish the PBL from the free atmosphere.

To verify the PBLHs retrieved from CALIPSO employing the new method, PBLHs from the microwave radiometer were obtained for comparison. We collected overlapping datasets with RPG and CALIPSO over the entire experimental period. Fig. 3 shows the results of linear regressions between CALIPSO_PBLHs and RPG_PBLHs for cloudy and cloud-free cases. In Fig. 3a, the correlation coefficient R^2 is 0.55 and CALIPSO-PBLHs are far greater than RPG-PBLHs in some cases. The RPG_PBLHs are estimated based on temperature profiles, while the CALIPSO_PBLHs are based on the attenuated backscatter, which may explain the differing results. In a study by McGrath-Spangler and Denning (2013), > 72% of stations had a difference of < 40% between CALIPSO-PBLHs and AMDAR-PBLHs (also based on temperature profiles). Some of the disagreement may be random and is possibly caused by space/time average errors (Stull, 1988). In some cases, especially during the summer, strong convection encourages lower-level cloud bases to remain close to or within the PBL. The formation and development of stratocumulus clouds can be driven by capped inversion. Under such scenarios, there would be little variation in θ within the clouds (Stull, 1988). Multiple cloud layers are difficult to be interpreted in CALIPSO data, potentially causing higher cloud layers to be identified as PBLHs (McGrath-Spangler and Denning, 2013). In this study,

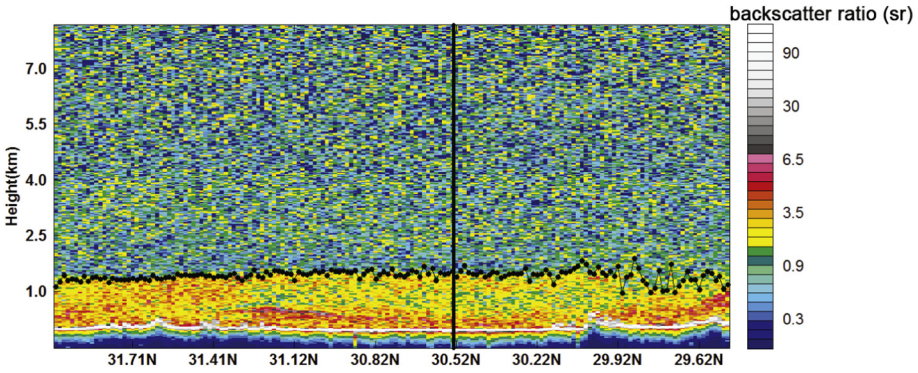

Fig. 2. CALIPSO attenuated ratio 2D intensity and the PBLH using the wavelet-curve fitting algorithm (the vertical black solid line represents the location of Wuhan City).

aerosol concentration profiles reflected by CALIPSO could have mistaken cloud tops as PBLHs during the formation of stratocumulus clouds. Fig. 3b illustrates that, when the above scenario is eliminated, the correlation coefficient R^2 increases to 0.86, which implies that the methods adopted in this study are reasonably robust and accurate.

4.2. Interannual and seasonal variation characteristics of CALIPSO_PBLH above Wuhan

To analyze the interannual characteristic of PBL in Wuhan, the monthly averages and their standard deviations, and sample size in all sky condition in each year during the study were calculated and summarized in Fig. 4. The sample size in different month varies between 10 and 60, which depends on the sky condition. The monthly averaged PBLHs of a small sample show relatively less representative and reference value. There is lack of valid detection in spring and summer when thick clouds tending to appear, causing the laser to fail to detect ground and returning no signal, or improving the probability of misinterpreting the cloud as PBL then leading to invalid results. It can be seen from Fig. 4 that the CALIPSO_PBLHs over Wuhan exhibit apparent interannual variations for the period of June 2006 to September 2013.In each year, the monthly averages of PBLH increase first and then decrease, resulting in the average values peaking in warmer month and lowest in colder month. The PBLH in summer is higher than other seasons with average range between 1300 and 1900 m in the daytime and 500–900 m in the nighttime, while the PBLH in winter is the lowest with average range between 800 and 1100 m in the daytime and 300–650 m in the nighttime. The reason can be that thermodynamic convection within the PBL is most vigorous in warmer months, which results in deeper PBLHs. The PBLHs in daytime are around 300–1000 m higher than in the nighttime, because of weaker convection in nighttime leading to more stable PBL. Some abnormally averaged values not conforming to this trend, are induced by less sample and relatively large standard deviation of the mean to some extent.

Tables 1 and 2, respectively, list the mean values and sample size of CALIPSO_PBLH in each season over Wuhan in the daytime and nighttime. The sample size in different season of different year varies between 10 and 130, which relies on the sky condition and weather. The sample size in summer is smaller than other seasons, due to the thick clouds appearing more frequent in summer leading to lack of valid signal. The seasonal averages of a limited sample are relatively less credibility with larger representation errors. The seasonal means of CALIPSO_PBLH in daytime are 1272 m, 1444 m, 1084 m, and 929 m for spring, summer, autumn, and winter, respectively, while the seasonal means in nighttime are 638 m, 671 m, 581 m, and 374 m. The summer (June, July, and August) value is the highest of the entire year, while the winter (December, January and February) value is the lowest of the entire year. McGrath-Spangler and Denning stated that extratropical land generally shows deeper mixing during the summer and deep retrieved PBHs are evident, while the boreal winter is cold and the retrieved PBLHs are shallow (McGrath-Spangler and Denning, 2013). Their published mean CALIPSO_ PBLHs is about 1500 m during the summer, which is similar to ours. The annual means of CALIPSO_PBLHs in daytime are 1138 m, 1148 m, 1154 m, 1146 m, 1223 m, 1123 m, 1318 m, and 1339 m for 2006 to 2013, while the annual averages in nighttime are 550 m, 536 m, 586 m, 586 m, 526 m, 555 m, 600 m and 659 m.

Fig. 5 illustrates the relative frequency in four seasons and cumulative frequency distribution of CALIPSO_PBLHs. It can be seen that the peak value of PBLHs distributions in the daytime is at 800–1000 m and

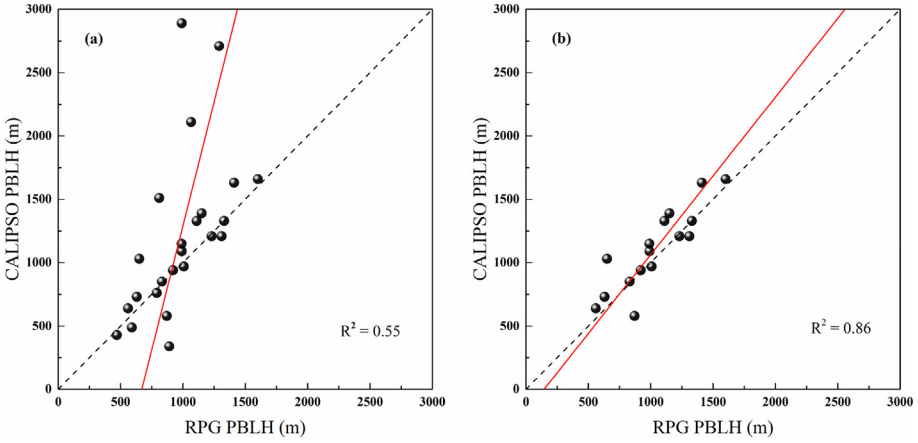

Fig. 3. R^2 values for the linear regressions between CALIPSO_PBLH and RPG_PBLH for (a) cloudy cases and (b) cloud-free cases, respectively.

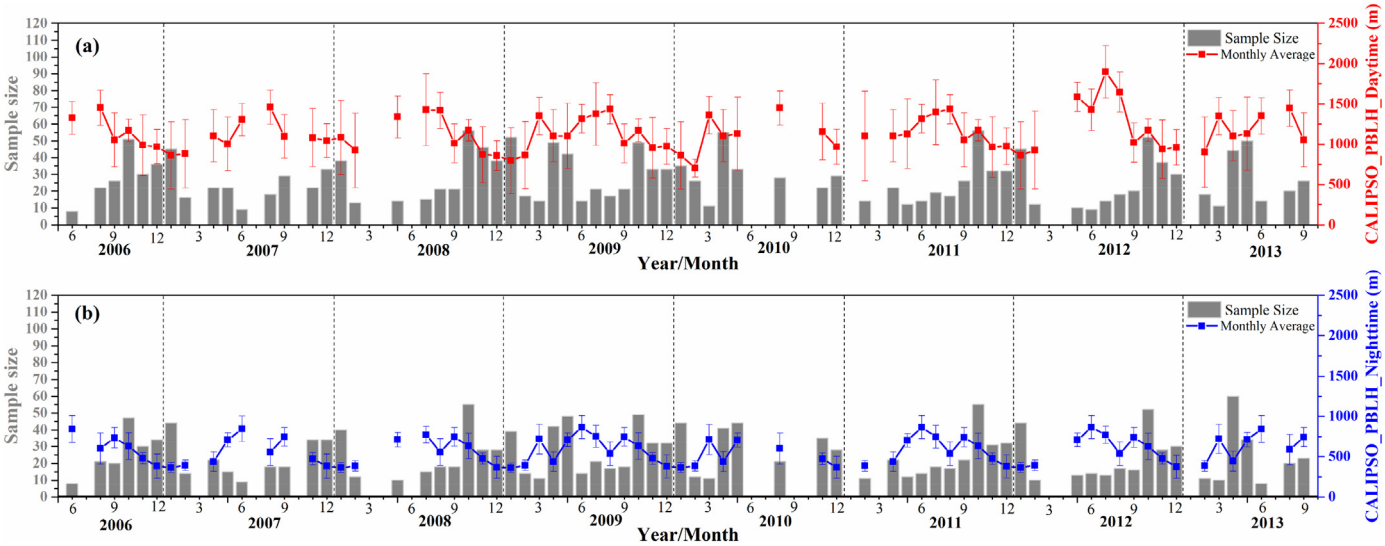

Fig. 4. Interannual variations of the CALIPSO_PBLHs and sample size in the daytime (a) and nighttime (b) from June 2006 to September 2013. The red or blue square points and its whiskers represent the monthly averages and standard derivation of CALIPSO PBLH. The gray columns represent the number of samples per month. (For interpretation of the references to colour in this figure legend, the reader is referred to the web version of this article.)

Table 1
Seasonal mean values and samples size of CALIPSO_PBLHs in the daytime above Wuhan. ("–" indicates that there is no available observation during the experimental period; units are in m).

Year	Spring		Summer		Autumn		Winter		Year_Mean	
	PBLH (m)	Samples	PBLH (m)	Samples	PBLH (m)	Samples	PBLH (m)	Samples	PBLH (m)	Samples
2006	–	0	1419	31	1091	108	903	98	1138	237
2007	1053	45	1408	28	1089	52	1044	85	1148	210
2008	1338	15	1421	37	1031	124	828	108	1154	284
2009	1266	106	1378	53	1069	104	873	95	1146	358
2010	1278	100	1450	29	1155	23	1011	44	1223	196
2011	1112	35	1386	51	1087	115	909	90	1123	291
2012	1587	11	1684	42	1065	110	937	49	1318	212
2013	1270	106	1409	35	–	0	–	0	1339	141
mean	1272	418	1444	306	1084	636	929	569	1182	1929

Table 2
Seasonal mean values and samples size of CALIPSO_PBLHs in the nighttime above Wuhan. ("–" indicates that there is no available observation during the experimental period; units are in m).

Year	Spring		Summer		Autumn		Winter		Year_Mean	
	PBLH (m)	Samples	PBLH (m)	Samples	PBLH (m)	Samples	PBLH (m)	Samples	PBLH (m)	Samples
2006	–	0	668	30	605	98	376	93	550	221
2007	548	38	653	28	568	53	374	87	536	206
2008	711	11	655	34	609	102	370	82	586	229
2009	657	104	712	53	603	100	373	89	586	346
2010	653	99	602	22	474	36	373	40	526	197
2011	531	35	708	50	609	109	373	87	555	281
2012	709	14	711	45	602	97	377	42	600	198
2013	656	105	661	29	–	0	–	0	659	134
mean	638	406	671	291	581	595	374	520	566	1812

the peak relative frequency is 22%, while the peak value of PBLHs distributes in the nighttime is at 400–600 m with the relative frequency of 30%. The relative frequency showed an approximately normal distribution with around 95% of the PBLHs clustered between 400 and 1800 m in daytime and 200–1000 m in the nighttime, i.e., very low or high PBLHs appear only rarely. Broad range in the daytime and narrow range in the nighttime indicate the more stable distribution of PBL in nighttime attributed to a relatively calm convection condition. Both in daytime and nighttime, PBL in warmer months distributes in higher altitude, while it clusters in lower altitude in colder month, in agreement with the results in Fig. 4, Table1 and Table 2, which ascribes to thermodynamic convection stronger in warmer month than in colder month. The relative frequency of all PBL in Fig. 5 (c), also shows an approximately normal distribution with about 95% of PBLHs clustering between 200 and 1800 m. PBLs in winter cluster in low elevation of 200–1200 m, while PBLs in other three seasons distribute between 200 and 1800 m with relatively uniform distributions, which should be related to the low solar radiation flux and weak turbulent energy in winter (Yang et al., 2016).

Fig. 6 (a) shows monthly variations of CALIPSO_PBLHs in the

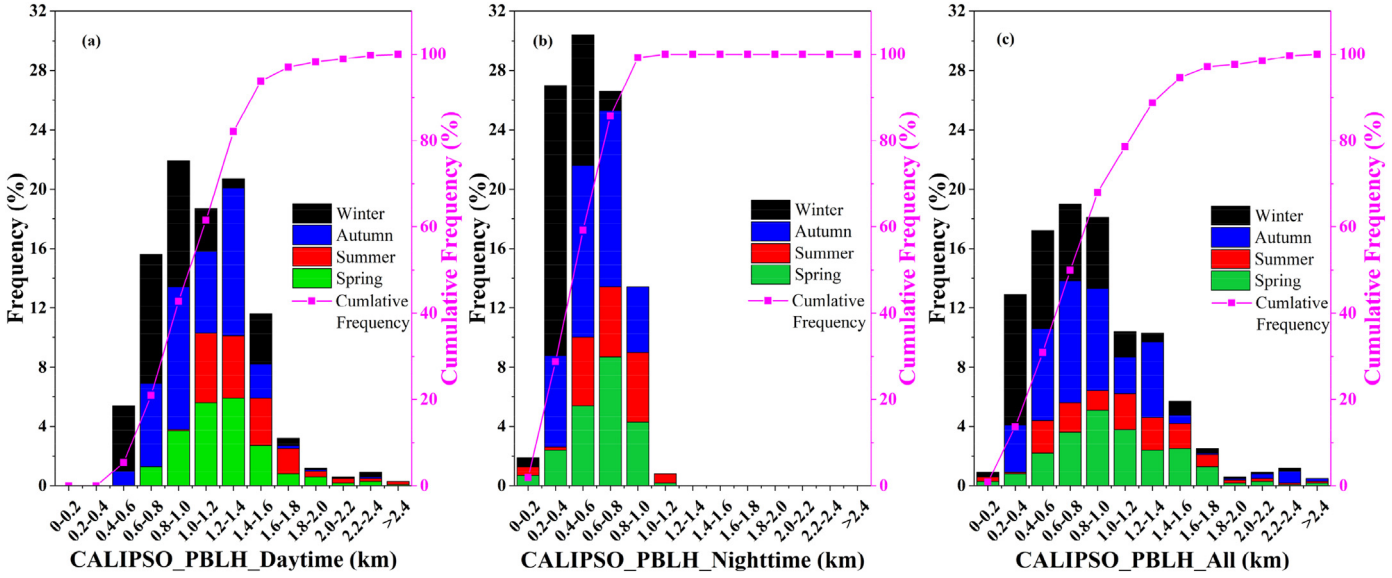

Fig. 5. Relative frequency in four seasons and cumulative frequency of CALIPSO_PBLHs over Wuhan in the daytime (a), nighttime (b) and all time (c) during our experimental period from 2006 to 2013. The magenta curve represents the cumulative frequency of CALIPSO PBLHs in different heights, while the green, red, blue, and black columns, respectively, are the relative frequencies of CALIPSO PBLH in different levels in spring (March, April and May), summer (June, July and August), autumn (September, October and November) and winter (January, February and December). (For interpretation of the references to colour in this figure legend, the reader is referred to the web version of this article.)

daytime. The monthly means of PBLH in the daytime range between 800 m and 1400 m; the mean maximum value occurs in August (1427 m), while the mean minimum value is observed in January (819 m), which is similar to the study of McGrath-Spangler and Denning using CALIPSO (McGrath-Spangler and Denning, 2013), with the mean maximum value occurring in June and the mean minimum value seen in December over land in the Northern Hemisphere. The PBLHs show significant seasonal variations with high values in spring and summer and low values in winter and autumn. Seasonal averages of PBLH are in following order: summer > spring > autumn > winter, with values of 1444 ± 291 m, 1272 ± 319 m, 1084 ± 277 m and 929 ± 349 m, respectively, in agreement with Kong's study in Wuhan with mean value of 1.27 km in summer, 1.24 km in spring, 1.13 km in autumn and 0.86 km in winter (Kong and Yi, 2015). Obvious monthly variations with relatively large amplitude indicate that PBLH is influenced by seasonal changes of solar radiation, and the intense solar radiation promotes the development of PBLH in summer while less solar radiation suppress the progress of PBLH in winter (Stull, 1988; Yang et al., 2016).

Monthly variations of PBLH in nighttime were also calculated and displayed in Fig. 6 (b). Relative to the daytime results, the mean values of PBLH at night are lower with the range between 300 m and 900 m. The maximum monthly average appears in June with values of 838 ± 162 m, while the minimum monthly averages occurs in December with value of 368 ± 134 m, which is similar to Zhu's experiment results that maximum monthly mean occurred in June and

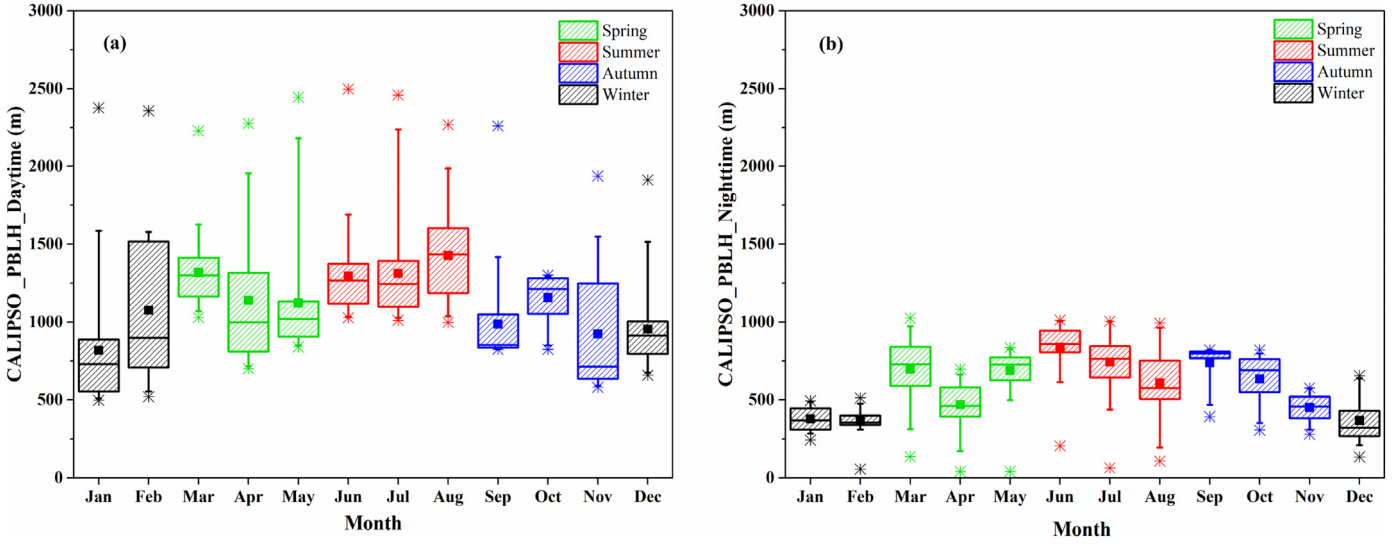

Fig. 6. Box-and-whisker plot of monthly variations of CALIPSO-PBLHs over Wuhan in the daytime (a) and nighttime (b). the plot shows the mean values (solid squares), median (horizontal bar in each box), 25th and 75th percentile (lower and upper ends of the boxes), 1 and 99th percentile (top and bottom lines), and maximum and minimum values (crosses) for different months. The whiskers show the standard deviations of the mean. Green boxes represent spring, red represent summer, blue represent autumn, and black represent winter. (For interpretation of the references to colour in this figure legend, the reader is referred to the web version of this article.)

minimum monthly mean was in December over Tianjin (Zhu et al., 2017), but the monthly distribution of PBLH could vary with location. Similar to daytime PBLH, seasonal averages of nocturnal PBLH follow the order: summer > spring > autumn > winter, with values of 671 ± 202 m, 638 ± 200 m, 581 ± 170 m and 374 ± 102 m, respectively. Because of the intense solar radiation and high surface temperature in summer over Wuhan, the atmosphere's convective motions are frequent and strong, favoring the diffusion of aerosol and pollutant, resulting in deeper PBLH in summer. Correspondingly, the aerosol particles and pollutants accumulated in near ground in winter due to slight solar radiation and low temperature, leading to low PBLH in cold season (Wang et al., 2016). The variation in monthly and seasonal mean of PBLH shows a significant quarterly dependence, which is reasonably consistent with the annual variation in the local surface temperature and seasonal variations of atmospheric pollution.

5. Conclusions

We used the complementary strengths of the ICF and WCT methods and employed them together to retrieve PBLHs based on CALIPSO attenuated backscatter ratios. The ICF method is more suitable for low vertical resolution and low SNR data, whereas the WCT method is more suitable for automated processing of large datasets. The method uses the WCT to obtain initial estimates for the ICF. The CALIPSO attenuated backscatter ratio signals eliminate the influence from air molecules, thereby highlighting the characteristics of the aerosols. Thus, the more vertically aligned shapes of the signals make the combined method algorithm easier to use. In addition, PBLHs from microwave radiometer measurements were obtained to verify the CALIPSO_PBLHs. For cloudy weather, the correlation coefficient R^2 is 0.55 and CALIPSO-PBLHs are far greater than RPG-PBLHs. When cloudy scenarios are eliminated, the correlation coefficient R^2 increases to 0.86, which implies that the methods adopted in this study are reasonably robust and accurate. CALIPSO_PBLHs over Wuhan exhibit apparent interannual variations for the period of June 2006 to September 2013, with the monthly averages of PBLH increasing first and then decreasing in each year, resulting in the average values peaking in warmer months and lowest in colder months. Over 90% of daytime CALIPSO_PBLHs are between 400 and 1800 m, while over 90% of nocturnal CALIPSO_PBLHs cluster between 200 m and 1000 m. Broad range in the daytime and narrow range in the nighttime indicate the more stable distribution of PBL in nighttime attributed to a relatively calm convection condition. The PBLHs in warmer seasons are higher than in cooler seasons, which can be attributed to the climatic characteristics of Wuhan. This research also offers a better understanding of the characteristics and mechanisms of the PBL over inland cities and helps to fill the gap in knowledge with regard to PBL processes in Wuhan. Furthermore, our results can provide PBLHs parameters for atmospheric models.

Acknowledgments

This study was supported financially by the National Key R&D Program of China (Nos. 2017YFC0212601, 2016YFC0200900), Hubei Provincial Natural Science Foundation of China (No. 2016CFB620), National Natural Science Foundation of China (No. 41571344), China Postdoctoral Science Foundation (No. 2015M572198), the Key Scientific Research Project of Henan Institutions of Higher Learning (Grant No. 18B170007), the Nanyang Normal University scientific research project (Program No. ZX2017014).

Author contributions

Miao Zhang and Zhongmin Zhu conceived and designed the experiments; Yusi Huang and Bo Zhu performed the experiments and analyzed the data; Yusi Huang, Tianhao zhang, Boming Liu and Ge Han checked the experimental data and examined experimental results; Zhongmin Zhu wrote the paper.

Conflicts of interest

The authors declare no conflict of interest.

References

Baars, H., Ansmann, A., Engelmann, R., Althausen, D., 2008. Continuous monitoring of the boundary-layer top with lidar. Atmos. Chem. Phys. 8 (23), 7281–7296.
Beyrich, F., Görsdorf, U., 1995. Composing the diurnal cycle of mixing height from simultaneous sodar and wind profiler measurements. Bound.-Layer Meteorol. 76, 387–394.
Bianco, L., Wilczak, J.M., 2002. Convective boundary layer depth: improved measurement by Doppler radar wind profiler using fuzzy logic methods. J. Atmos. Ocean. Technol. 19, 1745–1758.
Brooks, I.M., 2003. Finding boundary layer top: application of a wavelet covariance transform to lidar backscatter profiles. J. Atmos. Ocean. Technol. 20, 1092–1105.
Chen, J., Fan, S., Zhao, C., Xiao, X., Cai, X., Liu, H., 2006. The understanding of the turbulent fluxes in eddy correlation techniques. Chin. J. Atmos. Sci. 30 (3), 423–432.
Churnside, J.H., Stermitz, T.A., Schroeder, J.A., 1994. Temperature profiling with neural network inversion of microwave radiometer data. J. Atmos. Ocean. Technol. 11 (11), 105.
Cimini, D., De Angelis, F., Dupont, J.C., Pal, S., Haeffelin, M., 2013. Mixing layer height retrievals by multichannel microwave radiometer observations. Atmos. Meas. Tech. 6 (11), 2941–2951.
Compton, J.C., Delgado, R., Berkoff, T.A., et al., 2013. Determination of planetary boundary layer height on short spatial and temporal scales: a demonstration of the covariance wavelet transform in ground-based wind profiler and lidar measurements. J. Atmos. Ocean. Technol. 30 (7), 1566–1575.
Davis, K.J., Gamage, N., Hagelberg, C., Kiemle, C., Lenschow, D., Sullivan, P., 2000. An objective method for deriving atmospheric structure from airborne lidar observations. J. Atmos. Ocean. Technol. 17, 1455–1468.
Donnell, E.A., Fish, D.J., Dicks, E.M., Thorpe, A.J., 2001. Mechanisms for pollutant transport between the boundary layer and the free troposphere. J. Geophys. Res.-Atmos. 106, 7847–7856.
Emeis, S., Schäfer, K., Münkel, C., 2008. Surface-based remote sensing of the mixing-layer height – a review. Meteorol. Z. 17 (15), 621–630.
Feiyue, M., Wei, G., Yingying, M., 2012. Retrieving the aerosol lidar ratio profile by combining ground- and space-based elastic lidars. Opt. Lett. 37 (4), 617.
Flamant, C., Pelon, J., Flamant, P.H., Durand, P., 1997. Lidar determination of the entrainment zone thickness at the top of the unstable marine atmospheric boundary layer. Bound.-Layer Meteorol. 83, 247–284.
Garratt, J.R., 1994. The Atmospheric Boundary Layer. Cambridge University Press.
Garrett, T.J., Zhao, C., 2006. Increased arctic cloud longwave emissivity associated with pollution from mid-latitudes. Nature 440 (7085), 787–789.
Garrett, T.J., Zhao, C., Dong, X., Mace, G.G., Hobbs, P.V., 2004. Effects of varying aerosol regimes on low-level arctic stratus. Geophys. Res. Lett. 311 (17), 123–138.
Granados-Muñoz, M.J., Navas-Guzmán, F., Bravo-Aranda, J.A., Guerrero-Rascado, J.L., Lyamani, H., Fernández-Gálvez, J., Alados-Arboledas, L., 2012. Automatic determination of the planetary boundary layer height using lidar: one-year analysis over southeastern Spain. J. Geophys. Res.-Atmos. 117 (D18) (1984–2012).
Henne, S., Furger, M., Nyeki, S., Steinbacher, M., Neininger, B., Wekker, S.D., Dommen, J., Spichtinger, N., Stohl, A., Prévôt, A., 2004. Quantification of topographic venting of boundary layer air to the free troposphere. Atmos. Chem. Phys. 4, 497–509.
Jordan, N.S., Hoff, R.M., Bacmeister, J.T., 2010. Validation of Goddard earth observing system-version 5 merra planetary boundary layer heights using CALIPSO. J. Geophys. Res.-Atmos. 115 (D24), 9–12.
Kaufman, Y.J., Fraser, R.S., 1997. The effect of smoke particles on clouds and climate forcing. Science 277 (5332), 1636–1639.
Kong, W., Yi, F., 2015. Convective boundary layer evolution from lidar backscatter and its relationship with surface aerosol concentration at a location of a central China megacity. J. Geophys. Res.-Atmos. 120 (15), 7928–7940.
Korhonen, K., Giannakaki, E., Mielonen, T., Pfüller, A., Laakso, L., Vakkari, V., Baars, H., Engelmann, R., Beukes, J.P., Van Zyl, P.G., Ramandh, A., Ntsangwane, L., Josipovic, M., Tiitta, P., Fourie, G., Ngwana, I., Chiloane, K., Komppula, M., 2014. Atmospheric boundary layer top height in South Africa: measurements with lidar and radiosonde compared to three atmospheric models. Atmos. Chem. Phys. 14 (8), 4263–4278.
Krueger, A.J., Minzner, R.A., 1976. A mid-latitude ozone model for the 1976 U.S. standard atmosphere. J. Geophys. Res. Atmos. 81 (24), 4477–4481.
Leventidou, E., Zanis, P., Balis, D., Giannakaki, E., Pytharoulis, I., Amiridis, V., 2013. Factors affecting the comparisons of planetary boundary layer height retrievals from CALIPSO, ECMWF and radiosondes over Thessaloniki, Greece. Atmos. Environ. 74 (2), 360–366.
Li, S., Joseph, E., Min, Q., et al., 2016. Multi-year ground-based observations of aerosol-cloud interactions in the Mid-Atlantic of the United States[J]. J. Quant. Spectrosc. Radiative Transf. 188.
Liu, B., Ma, Y., Gong, W., et al., 2018. Determination of boundary layer top on the basis of the characteristics of atmospheric particles. Atmos. Environ. 178, 140–147.
Mao, F., Gong, W., Song, S., Zhu, Z., 2013. Determination of the boundary layer top from lidar backscatter profiles using a Haar wavelet method over Wuhan, China. Opt. Laser Technol. 49 (7), 343–349.
McGrath-Spangler, E.L., Denning, A.S., 2012. Estimates of north American summertime

planetary boundary layer depths derived from space-borne lidar. J. Geophys. Res.-Atmos. 117 (D15), 408–414.
McGrath-Spangler, E.L., Denning, A.S., 2013. Global seasonal variations of midday planetary boundary layer depth from CALIPSO space-borne lidar. J. Geophys. Res.-Atmos. 118 (3), 1226–1233.
Melfi, S., Spinhirne, J., Chou, S., Palm, S., 1985. Lidar observations of vertically organized convection in the planetary boundary layer over the ocean. J. Clim. Appl. Meteorol. 24, 806–821.
Morille, Y., Haeffelin, M., Drobinski, P., Pelon, J., 2007. STRAT: an automated algorithm to retrieve the vertical structure of the atmosphere from single-channel lidar data. J. Atmos. Ocean. Technol. 24 (5), 761–775.
Press, W.H., 1992. Numerical Recipes in Fortran 77: The Art of Scientific Computing. 1 Cambridge University Press.
Quick, A., 2004. Derivation Relating Altitude to Air Pressure. Portland State Aerospace Society. .
Russell, P.B., Hobbs, P.V., Stowe, L.L., 1999. Aerosol properties and radiative effects in the United States east coast haze plume: an overview of the tropospheric aerosol radiative forcing observational experiment (TARFOX). J. Geophys. Res. 104, 2213–2222.
Sawyer, V., Li, Z., 2013. Detection, variations and intercomparison of the planetary boundary layer depth from radiosonde, lidar and infrared spectrometer. Atmos. Environ. 79, 518–528.
Seibert, P., Beyrich, F., Gryning, S.-E., Joffre, S., Rasmussen, A., Tercier, P., 2000. Review and intercomparison of operational methods for the determination of the mixing height. Atmos. Environ. 34, 1001–1027.
Seidel, D.J., Ao, C.O., Li, K., 2010. Estimating climatological planetary boundary layer heights from radiosonde observations: comparison of methods and uncertainty analysis[J]. J. Geophys. Res.-Atmos. 115 (D16).
Seinfeld, J.H., Pandis, S.N., 2012. Atmospheric Chemistry and Physics: From Air Pollution to Climate Change. John Wiley & Sons.
Steyn, D.G., Baldi, M., Hoff, R., 1999. The detection of mixed layer depth and entrainment zone thickness from lidar backscatter profiles. J. Atmos. Ocean. Technol. 16, 953–959.
Stull, R.B., 1988. An introduction to boundary layer meteorology. Atmos. Sci. Libr. 8 (8), 89.
Su, T., Li, J., Li, C., Xiang, P., Lau, A.K., Guo, J., 2017. An intercomparison of long-term planetary boundary layer heights retrieved from CALIPSO, ground-based lidar, and radiosonde measurements over Hong Kong. J. Geophys. Res. 122.
Tang, G., Zhu, X., Hu, B., Xin, J., Wang, L., Münkel, C., Mao, G., Wang, Y., 2015. Impact of emission controls on air quality in Beijing during APEC 2014: lidar ceilometer observations. Atmos. Chem. Phys. 15, 12667–12680.
Tang, G., Zhang, J., Zhu, X., Song, T., Münkel, C., Hu, B., Schäfer, K., Liu, Z., Zhang, J., Wang, L., Xin, J., Suppan, P., Wang, Y., 2016. Mixing layer height and its implications for air pollution over Beijing, China. Atmos. Chem. Phys. 16, 2459–2475.
Twomey, S., 1977. The influence of pollution on the shortwave albedo of clouds. J. Atmos. Sci. 34 (7), 1149–1154.
Wallace, J.M., Hobbs, P.V., 2006. Atmospheric Science: An Introductory Survey. 92 Academic Press.
Wang, W., Gong, W., Mao, F., et al., 2016. An improved iterative fitting method to estimate nocturnal residual layer height. Atmosphere 7 (8), 106.
Wei, J., Tang, G., Zhu, X., Wang, L., Liu, Z., Cheng, M., et al., 2017. Thermal internal boundary layer and its effects on air pollutants during summer in a coastal city in North China. J. Environ. Sci. 70, 37–44.
Winker, D.M., Pelon, J.R., McCormick, M.P., 2003. The CALIPSO mission: Spaceborne lidar for observation of aerosols and clouds. In: Third International Asia-Pacific Environmental Remote Sensing Remote Sensing of the Atmosphere, Ocean, Environment, and Space. International Society for Optics and Photonics, Bellingham, WA, USA, pp. 1–11.
Winker, D.M., Hunt, W.H., McGill, M.J., 2007. Initial performance assessment of CALIOP. Geophys. Res. Lett. https://doi.org/10.1029/2007GL030135.
Wu, Y., Gan, C.-M., Cordero, L., Gross, B., Moshary, F., Ahmed, S., 2010. In PBL-height derivation from the CALIOP/CALIPSO and comparing with the radiosonde and ground-based lidar measurements. In: Remote Sensing. International Society for Optics and Photonics, pp. 78320C–78327.
Xie, S., Liu, X., Zhao, C., Zhang, Y., 2013. Sensitivity of cam5-simulated arctic clouds and radiation to ice nucleation parameterization. J. Clim. 26 (16), 5981–5999.
Yang, X., Zhao, C., Guo, J., Wang, Y., 2016. Intensification of aerosol pollution associated with its feedback with surface solar radiation and winds in Beijing. J. Geophys. Res.-Atmos. 121 (8), 4093–4099.
Yang, X., Zhao, C., Zhou, L., Wang, Y., Liu, X., 2017. Distinct impact of different types of aerosols on surface solar radiation in China. J. Geophys. Res.-Atmos. 121(11).
Zhang, W., Guo, J., Miao, Y., Liu, H., Zhang, Y., Li, Z., et al., 2016. Planetary boundary layer height from CALIOP compared to radiosonde over China. Atmos. Chem. Phys. 16 (15), 1–31.
Zhao, C., Garrett, T.J., 2015. Effects of arctic haze on surface cloud radiative forcing. Geophys. Res. Lett. 42 (2), 557–564.
Zhao, C., Xie, S., Klein, S.A., et al., 2012. Toward understanding of differences in current cloud retrievals of ARM ground-based measurements, AGU fall meeting. In: AGU Fall Meeting Abstracts, pp. 63–74.
Zhao C, Wang Y, Wang Q et al. A new cloud and aerosol layer detection method based on micropulse lidar measurements. J. Geophys. Res.-Atmos. 2014, 119(11).
Zhao, C., Qiu, Y., Dong, X., Wang, Z., Peng, Y., Li, B., et al., 2018. Negative aerosol-cloud re relationship from aircraft observations over Hebei, China. Earth Space Sci. 5, 19–29.
Zheng, C., Zhao, C., 2017. Analysis of influential factors for the relationship between PM2.5 and AOD in Beijing. Atmos. Chem. Phys. 19 (21), 1–57.
Zhu, X., Tang, G., Hu, B., Wang, L., Xin, J., Zhang, J., et al., 2016. Regional pollution and its formation mechanism over north china plain: a case study with ceilometer observations and model simulations. J. Geophys. Res.-Atmos. 121(24).
Zhu, X., Tang, G., Guo, J., Hu, B., Song, T., Wang, L., et al., 2017. Mixing layer height on the North China plain and meteorological evidence of serious air pollution in southern Hebei. Atmos. Chem. Phys. 1–21.